RESEARCH ARTICLE

A Non-PCM-Based 2 × 2 MIMO Antenna Array With Low Radar Cross-Section Using Characteristic Mode Analysis

MANZOOR ELAHI[1], **SLAWOMIR KOZIEL**[1,2], **(Fellow, IEEE), AND LEIFUR LEIFSSON**[3]

[1]Engineering Optimization and Modeling Center, Reykjavik University, 102 Reykjavik, Iceland
[2]Faculty of Electronics, Telecommunications and Informatics, Gdansk University of Technology, 80-233 Gdańsk, Poland
[3]School of Aeronautics and Astronautics, Purdue University, West Lafayette, IN 47907, USA

Corresponding author: Slawomir Koziel (koziel@ru.is)

ABSTRACT In this paper, we introduced a 2×2 multiple-input-multiple-output (MIMO) antenna array using a non-polarization conversion metasurface (NPCM) with reduced radar cross section (RCS). To achieve a low RCS, a chess-board configuration is typically adopted. However, in conventional NPCM designs, subarrays with 180° phase shifts apart exhibit radiating modes at different resonance frequencies due to varied unit cell sizes and spacing. To address this, a characteristic mode analysis (CMA) has been performed to investigate the radiation mechanism of each subarray, ensuring they resonate within the same frequency band. Through this analysis, the feeding structure was optimized based on the slot-coupled patch antenna theory to align the radiating modes of the subarrays within the desired bandwidth. Specifically, the fundamental mode TM_{01} of one subarray and higher order mode TM_{03} of the other were successfully excited to operate within the same frequency range. This configuration enables the low-RCS NPCM surface to implement a MIMO system in which each subarray radiates independently within the same frequency band. Full-wave simulations and measurements have been carried out to verify the performance of the proposed antenna array. The results indicate that the MIMO antenna maintains good isolation, ranging from 22 to 50 dB among ports within the operating band from 9.6 to 10.7 GHz, and exhibits RCS reduction under different polarization ranging from 9 to 19 dB across the band from 8.5 to 12 GHz. Moreover, the RCS under oblique incidence also demonstrate good performance, making it suitable for radar applications.

INDEX TERMS Non-polarizatoin conversion metasurface, Characteristic mode analysis, chess-board configuration, radar cross section, MIMO antenna.

I. INTRODUCTION

Radar cross section (RCS) reduction is crucial in modern warfare, especially for antenna arrays on low-observable platforms. Various methods, such as artificial magnetic conductors (AMC) [1], [2], metamaterial absorbers [3], [4], frequency selective surfaces (FSS) [5], and polarization conversion metasurfaces (PCM) [6], have been employed for this purpose. Recent advancements include coding metasurfaces that achieve broadband RCS reduction [7], [8], enhancing stealth capabilities.

Metamaterial-inspired antennas offer compact size, broad bandwidth, and high gain. In [9], a low-RCS antenna design with mushroom-like electromagnetic band-gap (EBG) structures is presented. Similarly, antenna arrays in [5], [10], [11], [12], and [13] employ linearly polarized (LP) elements to achieve circular polarization via sequentially rotated feeding networks. Moreover, the same feeding network is utilized in [14] for the circularly polarized array to enhance circular polarization.
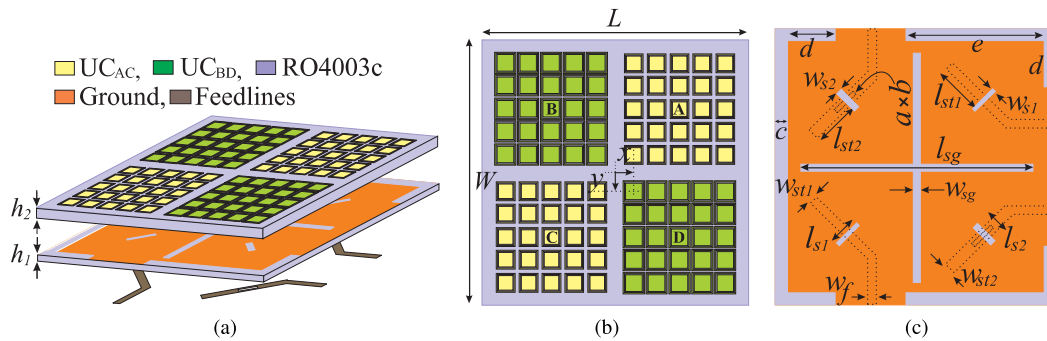
The associate editor coordinating the review of this manuscript and approving it for publication was Jagadheswaran Rajendran.

FIGURE 1. Geometry of the proposed 2 × 2 metasurface-based MIMO antenna design: (a) Split view. (b) Top layer. (c) Middle and bottom layer. [$L = W = 58$, $h_1 = 0.81$, $h_2 = 1.524$, $w_{s1} = 0.75$, $w_{s2} = 1$, $l_{s1} = 6$, $l_{s2} = 5.6$, $l_{st1} = 10$, $l_{st2} = 9.5$, $w_{st1} = 1.32$, $w_{st2} = 1.83$, $a = 4$, $b = 0.7$, $c = 2.5$, $d = 10$, $e = 28.5$, $l_{sg} = 48$, $w_{sg} = 1$, $w_f = 1.8$, $x = y = 3.46$]$_{mm}$.

Currently, MIMO antennas are essential for wireless communications, particularly in military applications such as UAVs and warships, providing high throughput [15] and low RCS for stealth operations. Reference [16] introduces a two-element MIMO configuration using FSS, achieving over 15 dB isolation and minimal in-band RCS reduction. Similarly, [17] and [18] propose two-element MIMO designs incorporating FSS as a ground plane, with [17] achieving 15 dB isolation in the 5–5.5 GHz band and 10 dB RCS reduction, while [18] operating from 2.12–2.24 GHz with RCS reduction in out-of-band frequencies from 6.5–14 GHz. A metasurface absorber (MA) in [19] and PCM in [20] are integrated with MIMO arrays. Reference [19] yields 15 dB Isolation in 8–12 GHz with 18 dB RCS reduction, while [20] achieves a 7 dB RCS reduction in the 4.4–8 GHz band. The work in [21] leverages purely PCM-based MIMO with 180° phase-shifted subarrays for reduced RCS. Each subarray is of the same size and excited with similar modes. In the aforementioned PCM-based arrays, each subarray acts both as a radiator and as a means to reduce RCS simultaneously. Implementing a MIMO array with reduced RCS using a PCM surface is relatively straightforward. Typically, a single subarray, designed to operate within a specific frequency band, is replicated to construct a MIMO array. All subarrays share identical dimensions and operating modes. However, this is not the case for NPCM-based MIMO arrays with reduced RCS, where variations in subarray design result in different operating modes. Therefore, NPCM-based array employs some subarrays of identical dimensions as radiators, while the others remain passive. For example, the chessboard configuration of the NPCM array in [22] utilized only two subarrays of the same size, excited with a single port instead of forming a MIMO array. The remaining two subarrays were left passive because their different dimensions resulted in resonant modes falling outside the desired frequency band. However, it would be advantageous to utilize all four subarrays of the NPCM-based array as radiating elements, achieving adequate RCS reduction within the desired bandwidth regardless of their different sizes.

This approach enables the realization of higher-order MIMO arrays based on NPCM-surface within a confined space.

This work introduces a four-port 2×2 MIMO antenna array structured in a chessboard arrangement, utilizing an NPCM where each subarray functions both as a low-scattering surface and an individual antenna radiator, regardless of the metasurface array's size. In such a layout, it is evident that subarrays that are 180° phase shift apart exhibit varying resonance frequencies due to differences in unit cell sizes and edge-to-edge spacing. Leveraging the theory of slot-coupled patch antennas, the resonant modes are achieved by adjusting the feeding structure. To elucidate the behavior of different radiating modes of individual metasurface arrays, a CMA is conducted, taking into account the parameters of each array's feeding structure. The analysis focuses on selecting specific modes: the TM_{01} mode of one subarray and the higher-order mode TM_{03} of another subarray are excited to radiate in the same frequency band while achieving reduced RCS. A prototype is fabricated and tested, showing good agreement with simulation results within the 9.6 to 10.7 GHz frequency band, with isolation levels ranging from 22 dB to a maximum of 50 dB across the entire band. Additionally, the design achieves substantial RCS reduction, ranging from 9 dB to 19 dB under different incident polarized waves across a wide bandwidth spanning from 8.5 to 12 GHz, which makes the design suitable for radar application.

II. DESIGN OF LOW-RCS MIMO ANTENNA ARRAY

Figure 1 illustrates the schematic diagram of the 2 × 2 metasurface-based MIMO antenna array, segmented into four sections. The identical metasurfaces within sections A and C are referred to as MS_{AC} while those in sections B and D are named MS_{BD}, featuring unit cells U_{AC} and U_{BD}, respectively. The metasurface is printed on the top layer of substrate-1 (1.524 mm thick Rogers RO4003C, $\epsilon_r = 3.38$) and four diagonally arranged slots are etched from the ground plane, which is printed on the bottom layer of substrate-I. The ground plane is sandwiched with substrate-II (0.81 mm thick RogersRO4003C, $\epsilon_r = 3.38$). Finally, the
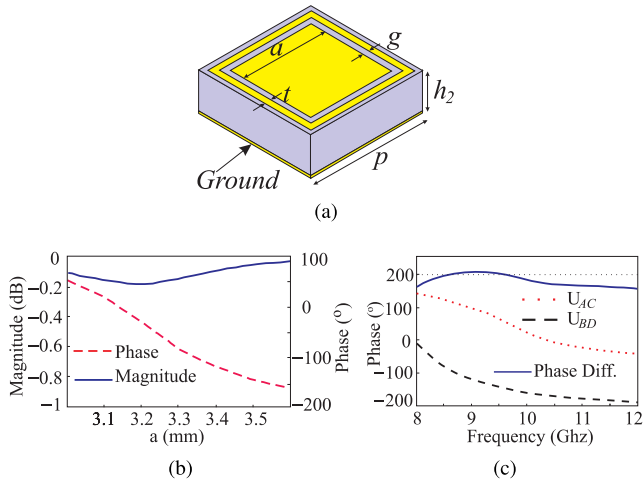
FIGURE 2. (a) Geometry of the unit cell. $[p = 5, t = 0.25, g = 0.25, h_2 = 1.524, a = \text{variable}]_{mm}$, (b) Simulated reflection magnitude and phase curves versus a of the unit cell at 10 GHz, (c) Simulated phase variations of the unit cells U$_{AC}$ and U$_{BD}$ and their corresponding phase difference versus frequency.
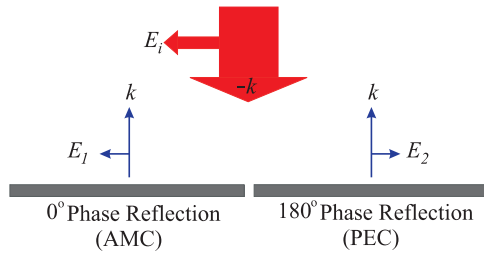

FIGURE 3. Scattering principle of the metasurface based array.

microstrip feedlines are printed on the bottom layer of substrate-II. Each section is fed by a separate microstrip-to-slot feeding structure located at the local centers. The identical sections A and C have similar feeding structures and similarly, sections B and D do the same. However, the two sets of sections vary in dimensions, as specified in the figure's caption. The feedlines to sections B and D employ rectangular slots for impedance matching. Additionally, a cross-shaped slot of dimensions $(l_{sg} \times w_{sg})$ is etched into the ground. MS$_{AC}$ and MS$_{BD}$ resonate at distinct frequencies due to different sizes and edge-to-edge spacings of the patch of unit cells. This section focuses on the step-by-step design of the NPCM-based MIMO antenna array where each subarray is resonating in the desired frequency band along with meeting the criteria of RCS reduction.

A. LOW RCS MECHANISM

RCS reduction is achieved through the appropriate arrangement of unit cells, which deviate incoming waves away from their original direction. Therefore, the reflection phase of the unit cells is an essential parameter that to be considered. A chess-board configuration is adapted along both the $x-$ and $y-axis$, featuring fixed-size unit cells with a phase difference $\Delta\phi = |\Delta U_{AC} - \Delta U_{BD}| \approx 180°$. To implement the
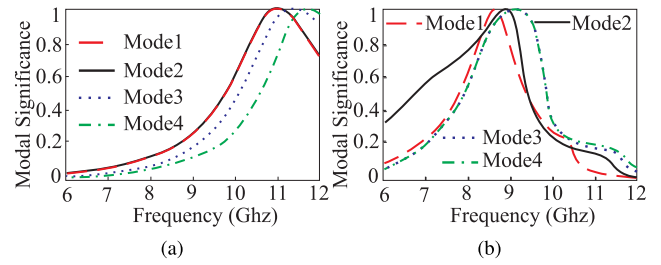

FIGURE 4. CMA results of the metasurfaces without feeding structure: (a) MS$_{AC}$ (b) MS$_{BD}$.

MS-based array, a simple unit cell structure containing a square patch inside a rectangular ring is adapted. The geometry of the unit cell is given in Figure 2(a). The unit cell is simulated at 10 GHz with a periodicity of 0.16λ. Figure 2(b) shows the phase reflection characteristics of the unit cell. Based on these plots, two unit cells U$_{AC}$ with $a = 3.09$ mm and U$_{BD}$ with $a = 3.59$ mm are chosen with phase reflection of 0° and 180°, respectively. Thus, the reflected waves from MS$_{AC}$ are out of phase with those from MS$_{BD}$, resulting a null in the broadside direction.

Theoretically, this phenomenon is explained as shown in Figure 3. The E-field E_i normally illuminates the two out-of-phase metasurfaces with 0° and 180° phase reflections, which behave as an artificial magnetic conductor (AMC) and a perfect electric conductor (PEC), respectively. Thus, the E-field reflected from the two metasurfaces E_1 and E_2 are given by:

$$E_1 = E_0 e^{j(wt-kr_1)} \tag{1}$$

and

$$E_2 = E_0 e^{j(wt-kr_2+\pi)} \tag{2}$$

where $w = 2\pi f$ and $k = 2\pi/r$, and r_1 and r_2 are the location of the point in the farfield along the broadside direction from the centers of metasurfaces where the E-field is to be calculated. E_1 has the same orientation as E_i, since there is no phase change after reflection from AMC surface. E_2 is out of phase with E_i due to reflection from PEC surface. From (1) and (2), the total reflected E-field E_t in the broadside direction given that $r_1 = r_2 = r$, using superposition theorem:

$$\begin{aligned} E_t &= E_0[e^{j(wt-kr_1)} + e^{j(wt-kr_2+\pi)}] \\ &= E_0 e^{j(wt-kr)}[1 + e^{j\pi}] = 0 \end{aligned} \tag{3}$$

From the above illustration, when a plane wave is incident on the metasurfaces, a null will appear in the broadside direction after refection from metasurface. In such a case, the main reflected beam splits into lobes away from the normal direction. For the proposed design, based on the periodicity of the unit cell columns, $\Gamma_x = \Gamma_y = 58$ mm along the $x-$ and $y-axis$, the incoming waves of wavelengths λ
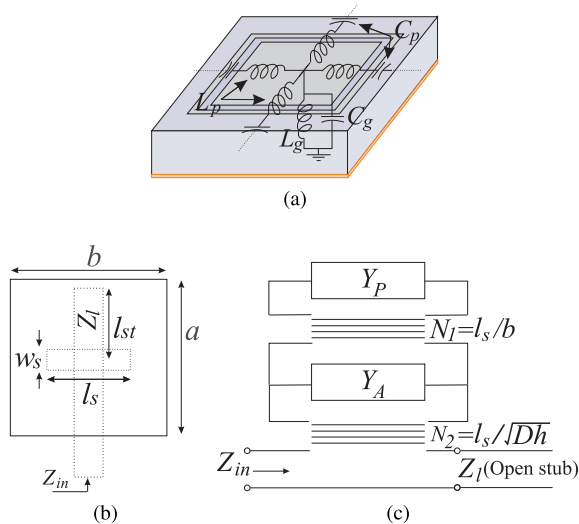
FIGURE 5. (a) Equivalent circuit model of the unit cell, (b) schematic diagram of the conventional slot-coupled MPA, (c) equivalent circuit model of the slot-coupled MPA.

at 10 GHz are scattered by an angle [23]:

$$\theta = sin^{-1}[\lambda\sqrt{\frac{1}{\Gamma_x^2} + \frac{1}{\Gamma_y^2}}] \qquad (4)$$

that is around 47°. To determine the RCS reduction bandwidth of the metasurface, the two unit cells U_{AC} and U_{BD}, must have the phase difference of approximately 180° within specific bandwidth. The phase difference bandwidth of the unit cell is shown in Figure 2(c). The phase difference between the two types of unit cells remains around 180°±25° in the frequency range of 8 GHz to 12 GHz.

B. RADIATION MECHANISM

The MS-based array serves not only as a low-scattering surface but also as a radiator. Following phase cancellation, the radiator design requirements must be addressed. Recently, CMA has gained prominence [24] for examining the radiation mechanisms of MS-based antennas. This study employs CMA at 6 GHz to analyze the radiation behaviours of two metasurface subarrays, MS_{AC} and MS_{BD}, both without feeding structures, as shown in Figure 4. For MS_{AC}, all four modes resonate above 11 GHz, while the modes for MS_{BD} are excited around 9 GHz. The differences in resonance frequencies are explained by the equivalent circuit model shown in Figure 5(a).

Reference [25] demonstrated that—with fixed unit cell periodicity—increasing the patch size quadratically increases the capacitance between the patch and ground (C_g), while inversely affecting the capacitance between the adjacent patches (C_p). This results in a lower resonant frequency. Conversely, reducing the patch size leads to a higher resonant frequency. Regarding the inductances, L_g depends only on the thickness of the dielectric, which is constant in this case and does not influence the resonant frequency. However, L_p
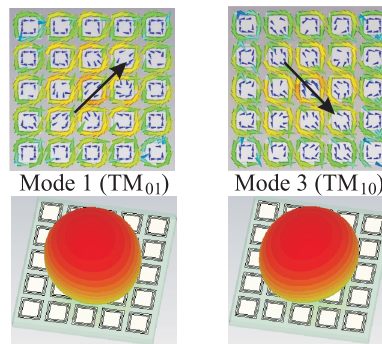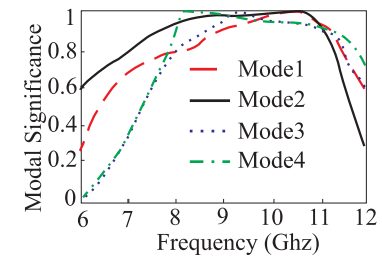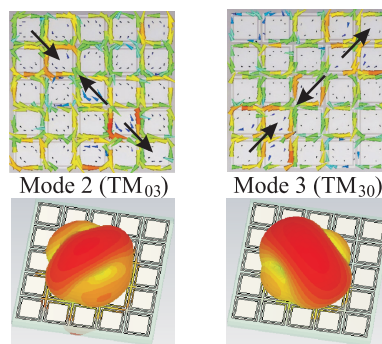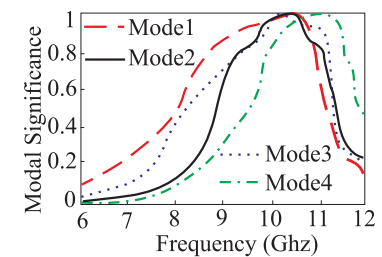
FIGURE 6. Modal significance, currents, and radiation patterns of modes on subarray including slot-coupled microstrip feedline: (a) TM_{01} at 10.3 GHz and TM_{10} at 10.4 GHz of MS_{AC}, (b) TM_{03} at 10.12 GHz and TM_{30} at 10.5 GHz of MS_{BD}.

is in a linear relationship with the patch size. Although the inductance L_p affects the resonant frequency, the capacitance plays a significant role. The modes in both antennas resonate at different frequencies, yet both MS-based arrays must radiate within the same frequency band. Adjusting unit cell sizes can tune radiation performance but impact scattering performance. To achieve effective radiation within the desired frequency band, feeding structure designs are necessary, as modifying the unit cell's structure or periodicity is not
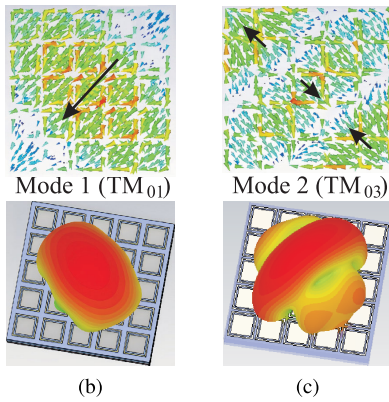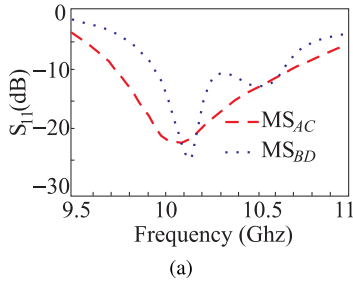
(a)

Mode 1 (TM$_{01}$)   Mode 2 (TM$_{03}$)

(b)   (c)

FIGURE 7. Performance of the MS-based subarrays using full-wave simulation: (a) Reflection coefficients of MS$_{AC}$ and MS$_{BD}$, (b) current distribution and radiation patterns of TM$_{01}$ mode at 10.3 GHz of MS$_{AC}$, (c) current distribution and radiation patterns of TM$_{03}$ mode at 10.12 GHz of MS$_{BD}$.

feasible. The metasurface antenna is electromagnetically coupled to the feed line via a rectangular slot, analogous to the slot-coupled microstrip patch antenna (MPA). The excitation of the resonant frequency through the feeding structure is clarified by the equivalent schematic and circuit model of the slot-coupled microstrip patch antenna, as depicted in Figure 5(b) and 5(c). Considering an open stub with characteristic impedance Z_l, length l_{st}, and wavenumber k_l on the microstrip line, the total input impedance Z_{in} is given by [26]:

$$Z_{in} = \frac{N_2^2}{N_1^2 Y_P + Y_A} - j Z_l cot(k_l l_{st}) \tag{5}$$

where N_1 and N_2 are the coupling coefficient from the aperture to MPA, the coupling coefficient from the feedline to aperture, respectively, and Y_P and Y_A are the input impedances of the MPA and the aperture. From the above illustration, it is evident that the mode can be excited in a specific frequency band by adjusting the parameters of the feeding structure. Following this concept, a CMA of the subarrays, incorporating the slot-coupled microstrip line, is performed to optimize feeding structure dimensions for exciting mode near 10 GHz. As shown in Figure 6, Mode 1 (TM$_{01}$) and Mode 3 (TM$_{10}$) of MS$_{AC}$ exhibit broadside radiation at 10.3 GHz and 10.4 GHz, while MS$_{BD}$'s higher-order modes−Mode 2 (TM$_{03}$) and Mode 3 (TM$_{30}$)−show broadside radiation with side lobes at 10.12 GHz and
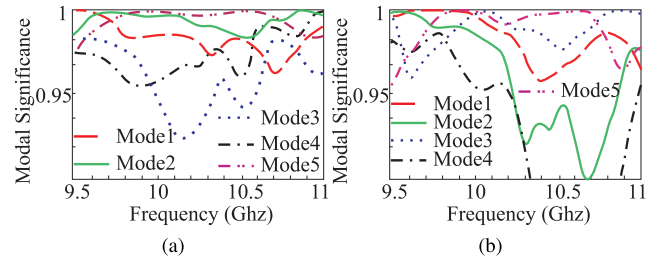

FIGURE 8. Modal significance of the 2 × 2 MS-based MIMO array: (a) without cross-shaped slot in the ground, (b) with cross-shaped slot in the ground.

10.5 GHz. The other modes exhibit a null in the radiation pattern at the broadside direction, which is not relevant in this case. For verification, full-wave simulated reflection coefficients of the individual subarrays are provided in Figure 7(a), effectively exciting Mode 1 and Mode 2 of MS$_{AC}$ and MS$_{BD}$, respectively, with current distribution and patterns are given in Figures 7(b) and 7(c). These results align with the selected characteristic modes' current and radiation patterns, confirming effective excitation through the optimized feeding structure.

To demonstrate the isolation between ports, a CMA analysis of the 2 × 2 MS-based MIMO array is carried out in CST. Figure 8 shows the modal significance of the first five modes of the array with and without a cross-shaped slot in the ground plane. The results indicate that in both cases the modal significance remains above 0.9. The model significance of each mode stays close to 1 across the wideband due to the combined effect of the two types of subarrays: MS$_{AC}$ and MS$_{BD}$. However, it is essential to characterize the behavior of these modes in terms of mutual coupling. The modal currents are plotted in Figure 9 for each mode on the ground plane at 10. 2 GHz. In Figure 9(a), without the cross-shaped slot, Mode 1 and Mode 4 exhibit a null in the center of the ground plane, indicating no coupling between the ports. However, diagonal current flow is observed crossing the center of the ground plane for Mode 2 and Mode 3, which indicates the mutual coupling between the two diagonally arranged ports. Mode 5 also shows the current between the two ports crossing the center of the ground plane, but the null point at the center of the feeding slots minimizes its contribution to coupling. Figure 9(b) presents the modal current distribution of the first five modes on the ground plane with cross-shaped slot. The insertion of the cross-shaped slot modifies the current distribution on the ground plane, preventing the direct current flow among the ports. Mode 1 and Mode 4 show null at the center of the ground plane due to cancellation of current vectors at the slot's center. Similarly, Mode 5 displays a null effect at the center of the ground plane, indicating no coupling. For Mode 2, the currents on the diagonal ports have the same direction, but there is no direct current crossing the center of the ground plane. The currents at the center of the slot effectively cancel out each other. Conversely, for Mode 3, the currents at the slot center are aligned in
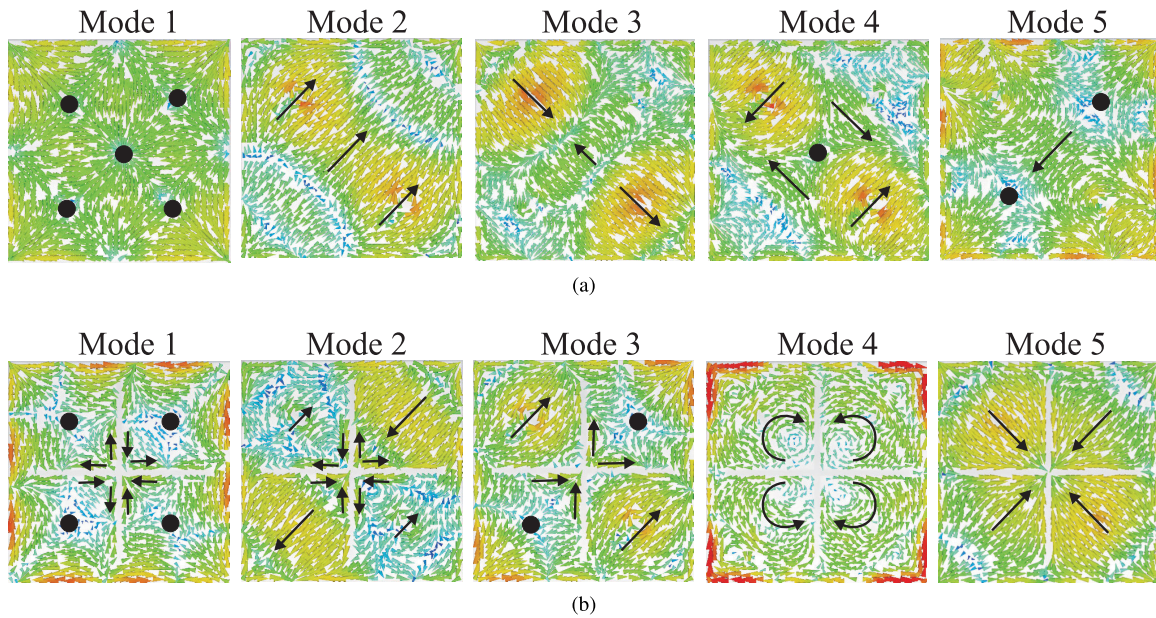
FIGURE 9. Modal currents distribution of first five modes at 10.2 GHz on the ground plane of the 2 × 2 MS-based MIMO array: (a) without cross-shaped slot in the ground plane, (b) with cross-shaped slot in the ground plane.
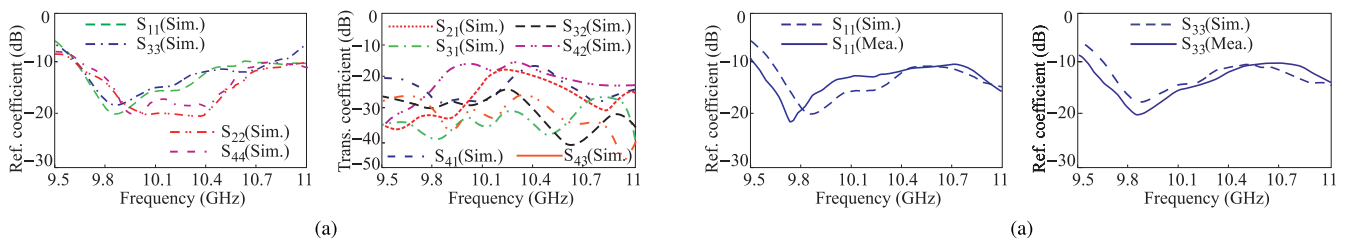

FIGURE 10. Simulated *S*-parameters of the MS-based MIMO array without a cross-shaped slot in the ground plane.
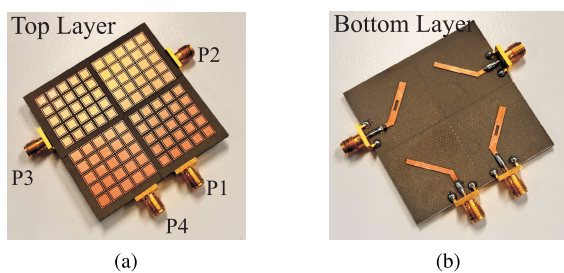

FIGURE 11. Prototype of the proposed 2 × 2 MS-based MIMO antenna design: (a) top layer, (b) bottom layer.

FIGURE 12. Comparison of simulated and measured *S*-parameters of the proposed 2 × 2 MS-based MIMO antenna: (a) reflection (Ref.) coefficients of Port 1 and Port 3, (b) reflection coefficients of Port 2 and Port 4, (c) Transmission (Trans.) coefficient among the four ports.

the same direction and do not cancel each other, suggesting potential coupling. However, a null appears at the feeding slot position, preventing coupling between the ports. For further illustration, the MS-based MIMO array is simulated without a cross-shaped slot in the ground plane. The simulated *S*-parameters of the array are presented in Figure 10. The reflection coefficients of each port remain below −10 dB in the bandwidth 9.6 GHz to 10.7 GHz. However, the mutual coupling between some ports is relatively high, around
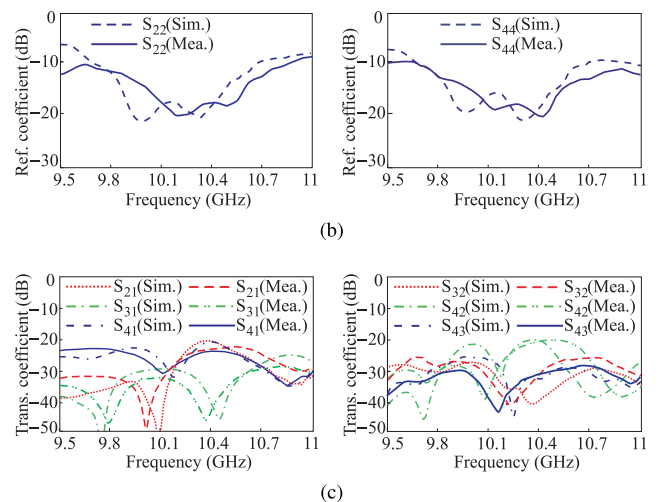
−15 dB across the bandwidth. The performance of the MS-based MIMO array with cross-shaped slot in the ground plane is discussed in detail in the next section.
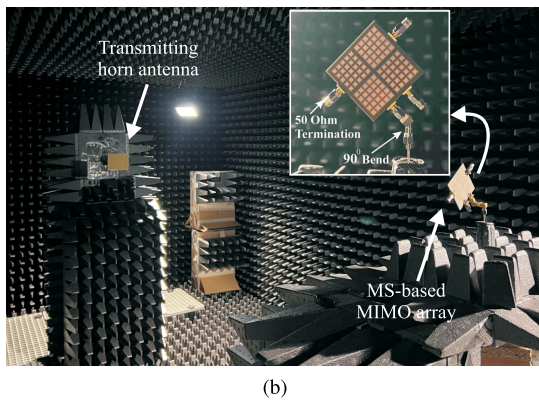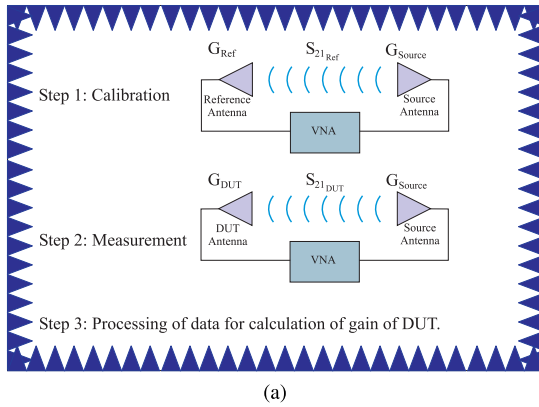
(a)

(b)

FIGURE 13. (a) Calibration and experimental setup for the gain measurement, (b) farfield measurement environment in the anechoic chamber at Reykjavik University.
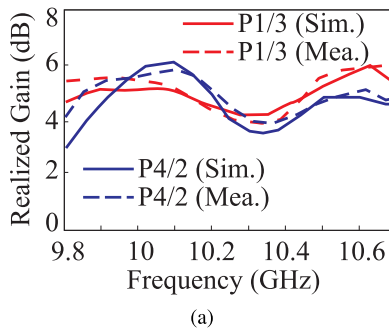

(a)

FIGURE 14. Comparison of simulated and measured realized gains of P1/3 and P4/2.

(a)

(b)

FIGURE 15. Comparison of simulated and measured radiation patterns of the proposed MS-based MIMO array at 10.2 GHz, (a) Port 1, (b) Port 4.

III. SIMULATION AND EXPERIMENTAL RESULTS

To assess performance, a MIMO array was fabricated, as shown in Figure 11. Each element of the 2×2 MIMO array is soldered with 50 Ω SMA connector. Figure 12 presents the simulated and measured S-parameters, demonstrating close agreement. The array operates effectively within the 9.6–10.7 GHz band, with minor discrepancies attributed to fabrication tolerances. Slight variations in the reflection and transmission coefficients of the identical sections A and C are due to asymmetrical ground truncation, which is also true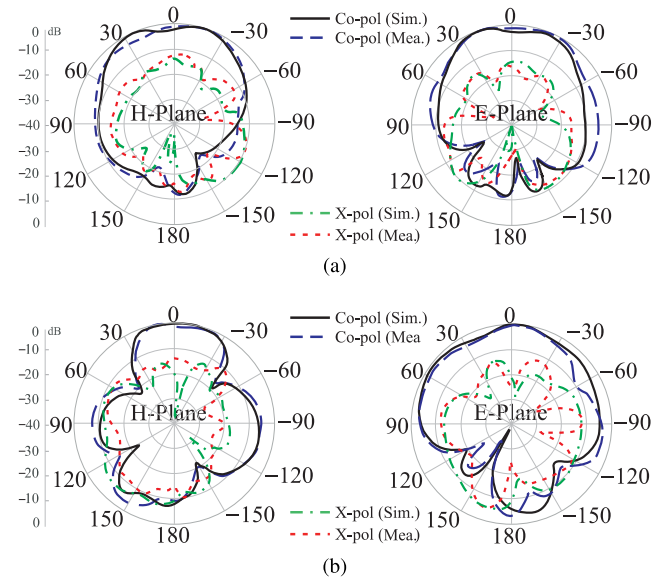 for sections B and D. Nonetheless, port isolation remains satisfactory, higher than 22 dB across the bandwidth with maximum of 50 dB. The farfield measurement is carried out in an anechoic chamber at Reykjavik University. Figure 13(a) shows the block diagram of the experimental setup for the calibration and gain measurements. The setup consists of a vector network analyzer (VNA), two linearly polarized horn antennas (BS0240DRH), and the device under test (DUT)—a prototype of the structure to be measured. First, the source and reference horn antennas are connected to the VNA for calibration. The reference antenna has precisely characterized gain, with accurate gain values provided in the datasheet. Initially, the signal strength, denoted as $S_{21_{Ref}}$, is measured across the frequency range of interest using the reference antenna, and calibration is performed. Next, the reference antenna is replaced with the DUT, and the same measurements are repeated to obtain the received signal strength, denoted as $S_{21_{DUT}}$. Finally, the gain of the DUT is calculated from the signal strengths $S_{21_{Ref}}$, $S_{21_{DUT}}$, and the gain of the reference antenna G_{Ref}, using the following formula:

$$G_{DUT} = S_{21_{DUT}} - S_{21_{Ref}} + G_{Ref} \qquad (6)$$

The far-field measurement environment in the Anechoic chamber is shown in Figure 13(b). The broadside far-field realized gains are measured and a comparison of simulated and measured gains versus frequency are plotted for Port 1/Port 3 (P1/3) and Port 4/Port 2 (P4/2) in Figure 14. A peak gain of 5.5 dBi and 6 dBi, respectively, have been achieved. The difference in gain between P1/3 and P4/2 is due to different excited modes—TM_{01} and TM_{03}, respectively. Moreover, the dip in the farfield plot can be seen around 10.3 GHz. There are two different MS-based surfaces of different sizes operating in the same frequency band with different modes. Each mode exhibits a unique field
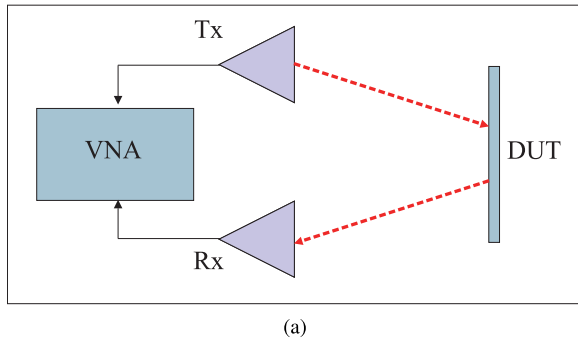
(a)

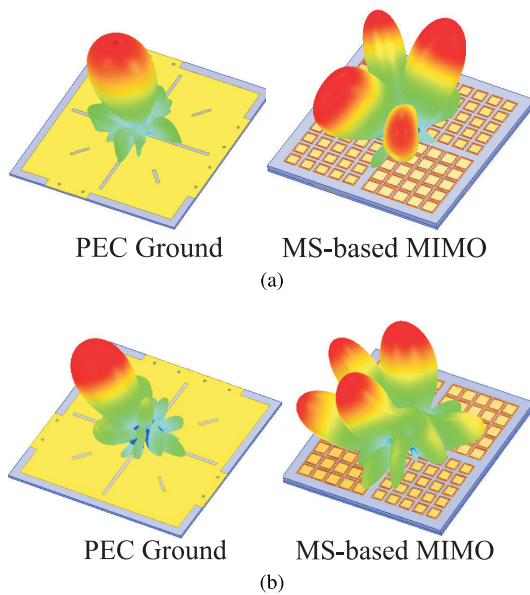**FIGURE 16.** Block diagram of the physical environment for the RCS measurement.

PEC Ground   MS-based MIMO

(a)

PEC Ground   MS-based MIMO

(b)

FIGURE 17. 3D scattering patterns of the PEC ground and MS-based MIMO array at 10.2 GHz at: (a) 0° incidence, (b) 30° incidence.

(a)   (b)

FIGURE 18. Simulation results of (a) RCS for different polarizations under normal incidence and (b) specular direction RCS reduction at different incidence angles.

FIGURE 19. Comparison of simulated and measured RCS of the PEC ground and MS-based array under normal incidence.

distribution. In the case of the TM_{01} mode, the maximum current intensity occurs at the center of the radiator, whereas for the TM_{03} mode, there are three maxima along the diagonal axis of the radiator. The radiated field depends on the currents on the active subarray and the currents on the coupled subarrays. For instance, if the excited and non-excited subarrays have the same dimensions and operating modes, the interference of the currents on the active subarray and the coupled subarray is uniform across the bandwidth. However, in the proposed structure, the active mode on the excited subarray tends to induce currents on the non-excited subarray that are not uniform throughout the band due to different characteristic modes. Thus, the interference of the lower and higher-order modes is sometime partially constructive and sometime partially destructive. The dip in gain around 10.3 GHz can be attributed to the field generated from partial out-of-phase currents on the active and the coupled subarrays. Moreover, the discrepancy between the measured and simulated gains can be attributed to the inclusion of
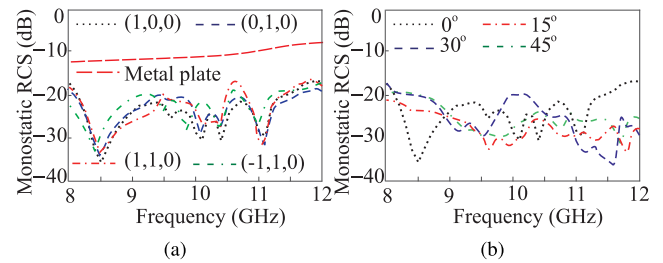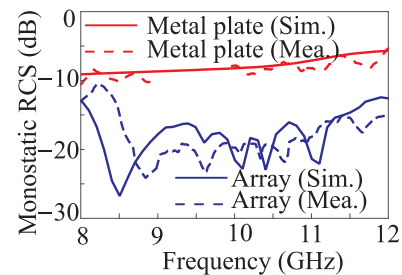
the 50 Ω terminations and the two-stage 90° bends during measurements. These factors cause the main lobe of the antenna to deviate slightly from the broadside direction, an effect that remains consistent across all frequencies in the band. The normalized simulated and measured patterns for Ports 1 and 4 at 10.2 GHz in both E-plane and H-plane are shown in Figures 15(a) and 15(b). Both ports exhibit broadside radiation with acceptable cross-polarization levels. Port 4 shows minor side lobes in the H-plane, consistent with the CMA pattern of TM_{03} in case of MS_{BD}. For Ports 3 and 2, the radiation patterns are similar to those of Ports 1 and 4, respectively, but with reciprocal patterns. Slight discrepancies between measured and simulated results are attributed to the effects of a 90° bend, 50 Ω loads, and metal components used during measurements.

The RCS has been measured in terms of reflectivity due to limited available sources. The metallic ground without meta-surface was used as a reference to evaluate the RCS reduction achieved by the proposed structure. For the measurements, two BS0240DRH horn antennas, operating from 2 GHz to 40 GHz, were employed as the transmitter and receiver. To ensure a normal incidence of the impinging waves on the structure, the antennas were positioned vertically relative to the surface under test. The distance between the antennas and the proposed structure was carefully maintained to satisfy far-field conditions. A block diagram of the measurement setup is shown in Figure 16. The scattering performance of the surface under test was evaluated through the antenna transmission coefficient, measured using a VNA. Similarly, the reflection from a metallic ground plane without the

TABLE 1. Comparison of the proposed 2×2 MS-based MIMO antenna array with previous works.

[Ref.]	RCS Tech.	Type	Substrate	metal type	size (λ_0^3)	MIMO elements & excited modes	PEC layer /air gap	Frequency band	Max. Isl (dB)	In-band RCS reduction (dB)
[16]	Slotted ground as FSS	2 port MIMO	FR4	—	0.53× 0.53× 0.03	Identical elements/ similar modes	2/No	3.7–9 GHz (83.4%)	15	Negligible
[17]	Slotted ground as FSS	2 port MIMO	FR4	Copper	0.7×0.6× 0.0.023	Identical elements/ similar modes	2/No	4.25–4.48 GHz (5.2%)	27	Negligible
[18]	Slotted ground as FSS	2 port MIMO	FR4	—	0.41×0.35× 0.011	Identical elements/ similar modes	2/No	2.05–2.15 GHz (4.7%	15	Negligible
[19]	MA integrated with array	2 port MIMO	FR4	Copper	2.65×2.65×0.42	Identical elements/ similar modes	2/Yes	8–12 GHz (40%	20	18
[20]	PCM integrated with array	2 port MIMO	FR4	Copper	2×1× 0.06	Identical elements/ similar modes	2/No	4.4–8 GHz (58%)	46	7
[21]	PCM-based array	4 port MIMO	RO4003C	Copper	1.65×1.65×0.103	Identical elements/ similar modes	2/No	7.56–7.93 GHz(4.7%)	20	11
[22]	Chess-board NPCM-based array	Single port Array	F4B	Copper	1.65×1.65×0.17	Identical elements/ similar modes	4/No	5.1–9 GHz (55%)	—	11
[Prop.]	Chess-board NPCM-based array	4 port MIMO	RO4003C	Copper	1.9×1.9×0.07	TM_{01} mode in one subarray's set and TM_{03} in other, excited in the same bandwidth	2/No	9.6–10.7 GHz (10.8%	50	9–19

Max. Isl: Maximum Isolation

metasurface was measured for comparison. Figure 17 shows the 3-D scattering patterns of the proposed antenna array and a reference ground metallic plate at different incidence angles at 10.2 GHz. In simulation, a linearly polarized plane wave is illuminated at the aperture in both cases. It can be seen that the scattered energy of the metallic ground is concentrated in the specular reflection direction, while the scattered energy of the proposed MS-based array splits into four lobes, resulting in a lower RCS. Due to the polarization-independent response of the unit cells, the proposed chessboard configuration of the MS-based MIMO array has a significant RCS performance under normal incidence with all polarizations. Figure 18(a) shows the RCS for different polarization, which clearly demonstrated that MIMO array is independent of polarization. Figure 18(b) shows the RCS reduction in broadside direction of the MIMO array at various incident angles. The RCS at incident angles other than 0° is high at low frequencies and low at higher frequencies in the bandwidth. However, the overall performance is gradually deteriorated as the incident angle increases. Figure 19 compares the simulated and measured RCS of the PEC ground and the proposed MS-based array across the band. The array demonstrates excellent measured performance from 8.5 to 12 GHz. Simulation and measurement results show good agreement. The slight difference in the measurement and simulated RCS performance can be attributed to the fabrication tolerances, as well as the misalignment of the transmitter/receiver antenna with respect to metasurface during measurements.

Table 1 benchmarks the proposed MIMO array design against contemporary MIMO arrays from the literature. References [16], [17], and [18] utilize FSS as a ground for RCS reduction and port isolation in 2 × 1 MIMO array. However, there is negligible in-band RCS redution. However, only 15 dB and 27 dB isolation have been reported in these papers. A 2 × 1 MIMO array with MA in [19] achieves 15 dB isolation and 18 dB RCS reduction in 8–12 GHz band, albeit with increased bulk. Similarly, a co-planar configuration of the MIMO array with PCM is proposed in [20], provides 46 dB isolation and 7 dB RCS reduction over 4.4–8 GHz.

The high isolation can be attributed to the truncated ground plane achieved at the expense of the directional radiation of the MIMO array. In the reviewed literature, MIMO arrays are integrated with either FSS, MA, or PCM, where the radiators and the integrated metasurfaces have individual contributions. Therefore, it is necessary to compare the proposed design with a metasurface-based MIMO array solely for fair comparison. Moreover, for simultaneous radiation and RCS reduction, a low-profile metasurface-based MIMO array is an optimal choice. Therefore, a PCM-based 2 × 2 MIMO array reported in [21] utilizes identical elements arranged orthogonally, resonating with similar modes. This allows a compact MIMO achieving an in-band RCS reduction of 11 dB and isolation around 20 dB. The design methodology is straightforward as the single metasurface-based element is replicated to implement the MIMO array. Unlikely, [22] introduces an NPCM-based 2 × 1 single-fed chess-board array, utilizing only two identical metasurfaces for the radiation, while the remaining metasurfaces are passive and contribute only to RCS reduction. It would be advantageous to utilize each section as a radiator as well as an RCS reduction element of an NPCM-based MIMO array, so that a dense MIMO array could be realized in a small area. In [16], [17], [18], [19], and [20], each element of the MIMO array radiates in the same mode and strict to the identical radiating structure. Similarly, [21] also presented PCM-based radiating structures with similar excited modes. In contrast, [22] kept the two NPCM-based elements excited, while the other two remained non-excited due to their resonance frequencies falling outside the desired frequency bands.

To avoid this issue, the proposed four port 2 × 2 MIMO array utilizes NPCM metasurfaces configured in chess-board geometry for the first time, in which each metasurface is simultaneously radiating in the same bandwidth and reducing RCS without considering the sizes of the subarrays. The advantage of the proposed work offers the opportunity that no matter what the sizes of the radiating elements, their respective modes can be adjusted to a specific bandwidth. Thus, each metasurface-based subarray of different sizes excited with different modes operating in the same band.

Overall isolation of less than 22 dB with isolation depth of 50 dB observed among the ports and excellent RCS reduction across the band with a maximum value of 19 dB, which make it a strong candidate for the radar application. Regarding size, each work listed in the comparison table, where the operating modes are determined solely by radiator dimensions, features smaller structures. The size of the proposed design is also compared with other metasurface-based MIMO arrays. However, increasing or decreasing the size of the MS-based array does not affect its RCS performance. The primary objective of the proposed design is to utilize the non-excited regions to realize a dense MIMO array using NPCM surface with reduced RCS, offering a distinct advantage over other NPCM-based MIMO arrays. Finally, the proposed design achieved a high isolation of 50 dB and a maximum in-band RCS reduction of 19 dB. Although the proposed design has small bandwidth but it marks a significant step toward compact NPCM-based MIMO arrays by disregarding the constraints of unit cell sizes and the overall metasurface radiator. In other words, this approach permits the construction of a compact and dense $n \times n$ array, where $n = 1, 2, 3, \ldots$, based on the outlined design procedure, regardless size and nature of metasurface used.

IV. CONCLUSION

In this paper, a new design approach has been proposed for a NPCM-based MIMO array characterized by low scattering performance. This is accomplished through a chessboard configuration and careful optimization of geometric parameters. Typically, NPCM configurations employ only subarrays of identical dimensions as radiators, while the remaining subarrays are kept passive due to different in size that lead to resonate in different frequency band. To increase the number of active radiating elements in MIMO array based on NPCM surface, each subarray should contibute to RCS and radiation simultaneously. Initially, a comprehensive CMA was performed on all subarrays, revealing that subarrays with high resonant frequencies have smaller unit cells and larger spacings, while subarrays with larger unit cells and closer spacings show lower resonance frequencies, exceeding bandwidth constraints. A subsequent CMA, including the feeding structure, ensured that the radiating modes efficiently operated within the desired bandwidth. This enables the creation of compact NPCM-based MIMO antennas using each subarray as a radiating element that leads to a dense MIMO array unlike the conventional NPCM-based MIMO array. Full-wave EM simulations and physical measurements of the antenna prototype confirm the design's effectiveness, showing excellent agreement between simulation and experimental results. The design achieved isolation levels between 22 dB and 50 dB across the target radar bandwidth of 9.6 to 10.7 GHz. RCS reduction is measured under linearly-polarized normal incident waves, which ranges from 9 dB to 19 dB over a frequency range of 8.5 GHz to 12 GHz.

REFERENCES

[1] M. F. El-Sewedy and M. A. Abdalla, "A monostatic and bistatic RCS reduction using artificial magnetic conductor metasurface," *IEEE Trans. Antennas Propag.*, vol. 71, no. 2, pp. 1988–1992, Feb. 2023.

[2] C. Vasanelli, F. Bögelsack, and C. Waldschmidt, "Reducing the radar cross section of microstrip arrays using AMC structures for the vehicle integration of automotive radars," *IEEE Trans. Antennas Propag.*, vol. 66, no. 3, pp. 1456–1464, Mar. 2018.

[3] Y. Han, L. Zhu, Y. Bo, W. Che, and B. Li, "Novel low-RCS circularly polarized antenna arrays via frequency-selective absorber," *IEEE Trans. Antennas Propag.*, vol. 68, no. 1, pp. 287–296, Jan. 2020.

[4] A. Bhardwaj, G. Singh, K. V. Srivastava, J. Ramkumar, and S. A. Ramakrishna, "Polarization-insensitive optically transparent microwave metamaterial absorber using a complementary layer," *IEEE Antennas Wireless Propag. Lett.*, vol. 21, no. 1, pp. 163–167, Jan. 2021.

[5] S. Zarbakhsh, M. Akbari, F. Samadi, and A.-R. Sebak, "Broadband and high-gain circularly-polarized antenna with low RCS," *IEEE Trans. Antennas Propag.*, vol. 67, no. 1, pp. 16–23, Jan. 2019.

[6] W. Yao, H. Gao, Y. Tian, J. Wu, L. Guo, and X. Huang, "Wideband low-RCS linear polarized array based on miniaturized polarization conversion metasurface," *IEEE Trans. Antennas Propag.*, vol. 71, no. 7, pp. 5663–5674, Jul. 2023.

[7] S. Koziel, M. Abdullah, and S. Szczepanski, "Design of high-performance scattering metasurfaces through optimization-based explicit RCS reduction," *IEEE Access*, vol. 9, pp. 113077–113088, 2021.

[8] M. Abdullah and S. Koziel, "Supervised-learning-based development of multibit RCS-reduced coding metasurfaces," *IEEE Trans. Microw. Theory Techn.*, vol. 70, no. 1, pp. 264–274, Jan. 2022.

[9] Y. Jia, Y. Liu, H. Wang, K. Li, and S. Gong, "Low-RCS, high-gain, and wideband mushroom antenna," *IEEE Antennas Wireless Propag. Lett.*, vol. 14, pp. 277–280, 2015.

[10] Y. Zhao, X. Cao, J. Gao, L. Xu, X. Liu, and L. Cong, "Broadband low-RCS circularly polarized array using metasurface-based element," *IEEE Antennas Wireless Propag. Lett.*, vol. 16, pp. 1836–1839, 2017.

[11] C. Zhang, J. Gao, X. Cao, L. Xu, and J. Han, "Low scattering microstrip antenna array using coding artificial magnetic conductor ground," *IEEE Antennas Wireless Propag. Lett.*, vol. 17, no. 5, pp. 869–872, May 2018.

[12] T. Hong, S. Wang, Z. Liu, and S. Gong, "RCS reduction and gain enhancement for the circularly polarized array by polarization conversion metasurface coating," *IEEE Antennas Wireless Propag. Lett.*, vol. 18, no. 1, pp. 167–171, Jan. 2019.

[13] W. Zhang, Y. Liu, and Y. Jia, "Circularly polarized antenna array with low RCS using metasurface-inspired antenna units," *IEEE Antennas Wireless Propag. Lett.*, vol. 18, no. 7, pp. 1453–1457, Jul. 2019.

[14] S. Karamzadeh, H. Saygin, and V. Rafiei, "Circularly polarized array antenna with emphasis on the reduction of RCS by utilizing semi-fractal elements," in *Proc. Int. Conf. Commun. (COMM)*, Bucharest, Romania, Jun. 2018, pp. 243–246.

[15] M. Elahi, J. Joung, and S. Lim, "Isolation and bandwidth enhancement in compact CP MIMO DRA in H-plane using Z-shaped strip," *IEEE Antennas Wireless Propag. Lett.*, vol. 18, no. 7, pp. 2700–2704, Jul. 2019.

[16] D. Gangwar, A. Sharma, B. K. Kanaujia, S. P. Singh, and A. Lay-Ekuakille, "Characterization and performance measurement of low RCS wideband circularly polarized MIMO antenna for microwave sensing applications," *IEEE Trans. Instrum. Meas.*, vol. 69, no. 6, pp. 3847–3854, Jun. 2020.

[17] S. R. Thummaluru, R. Kumar, and R. K. Chaudhary, "Isolation enhancement and radar cross section reduction of MIMO antenna with frequency selective surface," *IEEE Trans. Antennas Propag.*, vol. 66, no. 3, pp. 1595–1600, Mar. 2018.

[18] S. R. Thummaluru and R. K. Chaudhary, "Reducing the RCS of MIMO antenna using angularly stable FSS," in *Proc. URSI Asia–Pacific Radio Sci. Conf. (AP-RASC)*, Mar. 2019, pp. 42–52.

[19] G. Saxena, S. Kumar, S. Chintakindi, A. Al-Tamim, M. H. Abidi, W. A. M. Saif, S. Kansal, R. Jain, S. Singh, A. K. Dohare, P. K. Maduri, M. Kumar, H. Singh, and Y. K. Awasthi, "Metasurface instrumented high gain and low RCS X-band circularly polarized MIMO antenna for IoT over satellite application," *IEEE Trans. Instrum. Meas.*, vol. 72, pp. 1–10, 2023.

[20] P. Das and K. Mandal, "Polarization converter surface integrated MIMO antenna for simultaneous reduction of RCS and mutual coupling," *IEEE Antennas Wireless Propag. Lett.*, vol. 21, no. 9, pp. 1782–1786, Sep. 2022.

[21] S. Pandit, A. Mohan, and P. Ray, "Low-RCS low-profile four-element MIMO antenna using polarization conversion metasurface," *IEEE Antennas Wireless Propag. Lett.*, vol. 19, no. 12, pp. 2102–2106, Jul. 2020.

[22] L. Qiu and G. Xiao, "A broadband metasurface antenna array with ultrawideband RCS reduction," *IEEE Trans. Antennas Propag.*, vol. 70, no. 9, pp. 8620–8625, Sep. 2022.

[23] B. Fang, X. Bie, Z. Yan, H. Gan, C. Li, Z. Hong, and X. Jing, "Manipulation of main lobe number and azimuth angle of terahertz-transmitted beams by matrix-form-coding metasurface," *Appl. Phys. A, Solids Surf.*, vol. 125, no. 9, pp. 1–10, Sep. 2019.

[24] K. Wang, W. Shao, X. Ding, B.-Z. Wang, and B. Jiang, "Design of high-gain metasurface antenna based on characteristic mode analysis," *IEEE Antennas Wireless Propag. Lett.*, vol. 21, no. 4, pp. 661–665, Apr. 2022.

[25] L. O. Nur, A. Kurniawan, S. Sugihartono, and A. Munir, "Theoretical analysis of resonant frequency for AMC-based absorber composed of square patch array," *Int. J. Electr. Eng. Informat.*, vol. 7, no. 2, pp. 284–296, Jun. 2015.

[26] M. Himdi, J. P. Daniel, and C. Terret, "Transmission line analysis of aperture-coupled microstrip antenna," *Electron. Lett.*, vol. 25, no. 18, pp. 1229–1230, Aug. 1989.

SLAWOMIR KOZIEL (Fellow, IEEE) received the M.Sc. and Ph.D. degrees in electronic engineering from Gdansk University of Technology, Poland, in 1995 and 2000, respectively, the dual M.Sc. degree in theoretical physics and mathematics, in 2000 and 2002, respectively, and the Ph.D. degree in mathematics from the University of Gdańsk, Poland, in 2003. He is currently a Professor with the Department of Engineering, Reykjavik University, Iceland. His research interests include CAD and modeling of microwave and antenna structures, simulation-driven design, surrogate-based optimization, space mapping, circuit theory, analog signal processing, evolutionary computation, and numerical analysis.

MANZOOR ELAHI received the M.S. degree in electrical engineering from COMSATS University, Islamabad, Pakistan, in 2015, and the Ph.D. degree in electrical engineering from Sungkyunkwan University, Suwon, South Korea. Before pursuing his Ph.D., he was a Lecturer with the Department of Electrical and Computer Engineering, COMSATS University Islamabad, Pakistan. He is currently a Postdoctoral Researcher with the Department of Engineering, Reykjavik University, Iceland. Previously, he was a Postdoctoral Researcher with the Department of Electrical Engineering, Chung-Ang University, Seoul, South Korea. His research interests include MIMO antennas, circularly polarized antennas, reconfigurable dielectric resonator antennas, metasurfaces, and reflectarray antennas.

LEIFUR LEIFSSON received the bachelor's and master's degrees in mechanical engineering from the University of Iceland, Reykjavik, Iceland, in 1999 and 2000, respectively, and the Ph.D. degree in aerospace engineering from Virginia Tech, Blacksburg, VA, USA, in 2006. He is currently an Associate Professor of aerospace engineering with Purdue University, West Lafayette, IN, USA. His research interests include computational modeling, optimization, and uncertainty quantification of engineered systems with an emphasis on methods for multi fidelity modeling and machine learning. His application areas include aerodynamic shape optimization, aerodynamic flutter, model-based nondestructive evaluation, microwave devices, and food-energy-water nexus.

● ● ●